Next Materials 10 (2026) 101388

Contents lists available at ScienceDirect

Next Materials

journal homepage: www.sciencedirect.com/journal/next-materials

Research article

Influence of graphene oxide reduction and solvent effect on the performance of graphene oxide based supercapacitor

U.L.I. Udayantha [a], A.M.B.S. Alahakoon [a], A.D.T. Medagedara [b], J.A.C.P. Jayalath [a], G.R.A. Kumara [b], H.M.J.C. Pitawala [c], R.D.A.A. Rajapaksha [d], M.A.K.L. Dissanayake [b], T.M.W.J. Bandara [a,*]

[a] Postgraduate Institute of Science, University of Peradeniya, Sri Lanka
[b] National Institute of Fundamental Studies, Sri Lanka
[c] Department of Science and Technology, Uva Wellassa University, Sri Lanka
[d] Department of Nano Science Technology, Wayamba University of Sri Lanka, Sri Lanka

ARTICLE INFO

Keywords:
Energy density
Power density
Specific Capacitance
Dimethylformamide
Graphene Oxide
Reduced Graphene Oxide

ABSTRACT

Supercapacitors (SCs) hold significant promise as a key component in energy storage systems due to their unique combination of high-power density, rapid charge/discharge rates and long cycle life. Unlike traditional batteries, SCs can efficiently handle frequent charge/discharge cycles without significant degradation, making them ideal for applications requiring rapid energy delivery. Graphene oxide (GO) and reduced graphene oxide (RGO) are gaining significant attention as electrode materials for SCs due to their unique properties. The solvents, HNO_3 acid and DMF not only facilitate the dispersion of graphene-based materials but also impact the morphology, surface chemistry, and structural properties of the resulting thin films. The present research explores the suitability of GO and RGO-based composite electrodes prepared using 0.1 M HNO_3 acid and DMF for SCs. The reported work mainly focused on comparing the performance of RGO-based SCs with that of GO-based (control) using HNO_3 and DMF as solvents. The maximum specific capacitance obtained was 146 F g^{-1} at 2 mV s^{-1} for RGO – DMF-based SC at room temperature. The maximum gravimetric energy density of 21.58 Wh kg^{-1} and gravimetric power density of 81.55 kW kg^{-1} were exhibited for GO – DMF and RGO – DMF-based SCs, respectively. Electrochemical impedance analysis was used to characterize the device. Investigation of solvent influence on electrode preparation is unique and can provide insights into optimizing the electrode preparation process. The study uncovers that DMF is a better solvent for preparing GO and RGO-based electrodes. In addition, the study reveals that RGO-based SC shows higher performance compared to that of GO-based one.

1. Introduction

Climate change and the limited availability of fossil fuels and rapid fossil energy consumption have greatly affected the world economy and ecology and resulted in a series of serious problems such as large greenhouse gas emissions and environmental pollution. It is now essential that new, low-cost and environmentally friendly energy storage systems be found, in response to the needs of modern society and emerging ecological concerns [1]. Supercapacitors (SCs), also known as ultracapacitors or electrochemical capacitors, have garnered significant attention in the realm of energy storage due to their unique properties and numerous advantages. Unlike traditional batteries, SCs store energy through the separation of charge at the interface between an electrode and an electrolyte, enabling rapid charge and discharge cycles. This characteristic endows SCs with high power density, allowing them to deliver bursts of energy quickly, making them ideal for applications requiring rapid energy transfer such as regenerative braking in vehicles or peak power shaving in renewable energy systems [2,3]. Additionally, SCs exhibit excellent cycling stability. Moreover, their relatively simple design and use of environmentally friendly materials make them promising candidates for sustainable energy storage solutions [4]. The choice of electrode material plays a crucial role in determining the performance and efficiency of SCs. The specific surface area, conductivity, and electrochemical stability of the electrode material directly impact the capacitance, power density, and cycling stability of the SC [5]. GO and RGO have garnered significant attention as electrode

* Corresponding author.
E-mail addresses: awijendr@yahoo.com, wijendra@sci.pdn.ac.lk (T.M.W.J. Bandara).

https://doi.org/10.1016/j.nxmate.2025.101388
Received 12 July 2025; Received in revised form 27 October 2025; Accepted 28 October 2025
Available online 10 November 2025

materials for SCs due to their unique properties. GO, a precursor of graphene, possesses abundant oxygen-containing functional groups, which facilitate dispersion in aqueous solutions and enable easy processing into various forms. On the other hand, RGO, derived from GO through reduction processes, retains the sp^2 carbon structure of graphene while exhibiting improved electrical conductivity compared to GO [6,7]. Both materials offer high specific surface areas, allowing for enhanced ion adsorption and storage capacity within the electrode. Additionally, the tunable properties of GO and RGO, such as surface functionalization and layer thickness, provide avenues for tailoring the electrochemical performance of SCs [8]. In this study, GO and RGO were successfully synthesized from natural graphite powder using a modified Hummers method. The process involved the oxidation of graphite to produce GO, followed by the reduction of GO to obtain RGO. The reduction of GO to produce RGO is of paramount importance in enhancing the performance of SCs. The reduction process involves the removal of oxygen-containing functional groups from GO, leading to the restoration of sp^2 carbon networks similar to pristine graphene. This reduction significantly improves the electrical conductivity of the material, thereby reducing internal resistance and facilitating more efficient charge transfer kinetics within the electrode. As a result, RGO exhibits higher specific capacitance and lower equivalent series resistance compared to GO, leading to enhanced energy storage capabilities and improved electrochemical performance of SCs [9,10]. Moreover, the reduction of GO also results in an increase in surface area and porosity, providing more active sites for ion adsorption and thus further enhancing the capacitance of the electrode material [11]. Solvent is critical in the fabrication of GO and RGO thin films as electrode materials for SCs due to its significant impact on film quality, morphology, and electrochemical performance. The solvent not only affects the dispersion and stability of the GO suspension but also influences the reduction process and the final properties of the RGO film. A suitable solvent for processing GO should effectively exfoliate and stabilize GO sheets, enabling uniform dispersion and homogeneous deposition onto the substrate. Additionally, it should facilitate or not interfere with the reduction process by promoting the removal of oxygen-containing functional groups, thereby aiding in the restoration of the conjugated sp^2 carbon network. [12]. Additionally, the solvent's polarity, surface tension, and evaporation rate can influence the film's thickness, porosity, and crystallinity, thereby affecting the accessibility of active sites for ion adsorption and the overall capacitance of the SC electrode [13,14]. The selection of Dimethylformamide (DMF) and HNO_3 as solvents in the fabrication process of GO and RGO thin films for SC electrodes holds paramount importance. DMF, known for its high boiling point and excellent solvating properties, facilitates the dispersion of GO during the synthesis of GO, ensuring uniform coating and deposition onto the substrate. Furthermore, DMF serves as an effective medium for the reduction of GO to RGO, promoting the removal of oxygen-containing functional groups and the restoration of sp^2 carbon networks, thus enhancing the electrical conductivity and electrochemical performance of the resulting RGO thin films [15]. HNO_3, on the other hand, plays a crucial role in the oxidative treatment of graphite to produce GO precursor, initiating the formation of GO sheets by introducing oxygen functionalities. Moreover, HNO_3 treatment aids in the exfoliation and functionalization of graphite layers, leading to enhanced dispensability and reactivity of the resulting GO suspension [16]. The current collector serves as a foundation for the electrode material, facilitating efficient electron transport between the electrode and the external circuit [17]. FTO stands out as a highly advantageous current collector material for GO and RGO based SCs. FTO exhibits excellent electrical conductivity, ensuring efficient electron transport between the electrode material and the external circuit, thus minimizing energy loss and enhancing overall device efficiency. Furthermore, FTO demonstrates remarkable chemical stability and corrosion resistance, ensuring long-term durability and reliability of the SC device [18]. The electrolyte serves as the medium through which ions migrate between the electrodes during charge and discharge cycles, enabling the storage and release of electrical energy. Factors such as ionic conductivity, viscosity, and electrochemical stability are crucial considerations in selecting an electrolyte [19]. H_2SO_4 acid exhibits high ionic conductivity, facilitating the efficient transport of ions between the electrodes during charge and discharge cycles. This characteristic enables rapid energy storage and release, leading to high power density and fast response times [20].Modern improvements in GO - based materials have expanded their application potential in SCs. Modified GO with tailored oxygen functional groups has been shown to enhance ion accessibility and surface wettability, thereby improving capacitance and cycling stability. Structural engineering strategies, such as producing porous or three - dimensional architectures, further improve active surface area and facilitate fast ion transport. Hybrid composites of GO with metal oxides, conductive polymers, and heteroatom doping strategies have been widely investigated to boost energy density and conductivity while maintaining good mechanical stability [21]. RGO, produced through controlled thermal, chemical, or electrochemical reduction of GO, demonstrates a balance between oxygen functionalities and conductivity, enabling boosted charge transfer and better electrochemical performance. These advancements underscore the importance of fine-tuning GO's structural, chemical, and electronic characteristics to optimize its role as a high-performance electrode material for next-generation supercapacitors [22]. In this study, GO and RGO were synthesized from graphite powder via a modified Hummers method, followed by an investigation into the effect of different solvents, namely DMF and HNO_3 acid, on the reduction of GO and its subsequent impact on the performance of SCs. The reduction process is crucial as it influences the electrical conductivity and structural integrity of the resulting RGO, which directly affects the electrochemical properties of the SC. By systematically varying the solvent composition, we aim to elucidate the role of solvent in the reduction process and its implications for SC performance. This research sheds light on optimizing the synthesis parameters to enhance the energy storage capabilities and overall efficiency of graphene-based SCs, offering insights for the development of advanced energy storage devices.

2. Materials and methods

2.1. Synthesis of graphene oxide and reduced graphene oxide

Graphene oxide (GO) was synthesized using a modified Hummer's method, which is a widely adopted chemical route for the oxidation of graphite. Initially, 1 g of natural graphite powder and 0.5 g of sodium nitrate ($NaNO_3$) were mixed thoroughly in a beaker. To initiate the oxidation process, 13 ml of concentrated sulfuric acid (H_2SO_4, 98 %) was added slowly to the mixture while maintaining the temperature below 5 °C using an ice bath. Continuous stirring with a magnetic stirrer was employed during this step to ensure uniform dispersion and to prevent localized overheating.

Once the acid was completely added and the mixture was stabilized, 3 g of potassium permanganate ($KMnO_4$) was gradually added in small portions. The slow addition of $KMnO_4$ is critical to avoid a rapid increase in temperature and to maintain a controlled oxidation environment. After the complete addition of $KMnO_4$, the reaction mixture was kept at room temperature overnight to ensure oxidation of graphite into graphite oxide.

The next day, the resulting highly viscous mixture was carefully diluted with deionized water to a final volume of approximately 200 ml. To terminate the oxidation reaction and decompose any residual $KMnO_4$, 30 % hydrogen peroxide (H_2O_2) was added dropwise until the reaction mixture turned bright yellow, indicating the reduction process. This quenching step also helps in improving the safety and stability of the product.

The resulting greenish-yellow suspension, containing exfoliated graphene oxide, was subjected to purification to remove residual acids,

salts, and other by-products. For this the suspension was first filtered to remove unreacted solids and large agglomerates, followed by repeated washing with deionized water until a neutral pH was achieved, ensuring the removal of acidic impurities. It was then centrifuged to further isolate the well-dispersed GO. After this step, the suspension was divided into two portions to obtain both GO and reduced graphene oxide (RGO). One portion was retained as the GO suspension, while the other was further diluted with deionized water and subjected to a chemical reduction process to produce RGO, allowing both materials to be used in subsequent applications.

2.2. Fabrication of electrode

The pH value of two suspensions (GO and RGO) 100 ml (1 g/L) was tuned to 10 by gradually adding sodium hydroxide (NaOH). Then the mixture was heated to 95 ℃ and held for 2 h and it was sonicated for 30 min. The synthesis was performed at 95 °C and maintained for 2 h to ensure complete oxidation. Then the mixture was filtered and dried at 65 ℃ for 12 h in a vacuum oven. The 0.100 g of GO and RGO was mixed with 1 ml of 0.1 M HNO_3 acid and the mass of 0.100 g of GO and RGO was mixed with 1 ml of DMF separately. Then, 0.02 g of TiO_2 (20 % of GO and RGO) was added separately and the two solutions were sonicated for 3 h and then stirred for 24 h to reduce the particle size of graphene. The reduction process of GO to RGO was carried out under controlled heating and chemical treatment, followed by filtration and drying at 65 °C in a vacuum oven for 12 h to obtain stable RGO powder.

The electrode slurry was prepared by thoroughly dispersing either graphene oxide (GO) or reduced graphene oxide (RGO) in the solvent along with titanium dioxide (TiO_2), which serves as the binder. The dispersion process was carried out using vigorous stirring and sonication to ensure a homogeneous mixture with uniformly distributed particles. Once the slurry achieved a consistent texture, it was carefully drop-casted onto fluorine-doped tin oxide (FTO) glass substrates, which served as the current collectors. Special attention was given to ensure uniform spreading of the slurry across the substrate surface to promote consistent film thickness. Following the coating process, the electrodes were subjected to thermal drying in a hot air oven at 120 °C for one hour. This step ensured the complete evaporation of residual solvents, resulting in the formation of smooth, uniform thin-film coatings on the FTO substrates which was used for subsequent characterization or device fabrication.

2.3. Cell assembling

After preparing two identical electrodes, cells were assembled by sandwiching the electrolyte–impregnated filter paper, which also works as the separator. The entire stack was then sealed to prevent electrolyte leakage. To simulate practical application environments, each assembled symmetric two-electrode supercapacitor was developed using a planar configuration with a 1 cm^2 active electrode area and a 1 mm thick cellulose-based filter paper separator. The total electroactive material mass per cell was tested as 0.0052 g (GO-HNO_3) > 0.0028 g (GO-DMF) > 0.0024 g (RGO-DMF) > 0.0020 g (RGO-HNO_3), corresponding to 0.0026 g, 0.0014 g, 0.0012 g, and 0.0010 g per electrode, respectively. These values fall within the typical mass loading range of practical lab-scale supercapacitor devices and were used normally for all electrochemical measurements to make secure, reliable and comparable performance evaluation.

2.4. Electrochemical testing

Cyclic Voltammetry (CV) was performed between 0 – 1 V potential window at different scan rates, 2 mV s^{-1} to 100 mV s^{-1} at room temperature. In galvanostatic charge–discharge (GCD) testing, the SC was charged and discharged at a constant current and the voltage across the electrodes was monitored. GCD testing was done at different constant currents 0.5 mA cm^{-2} to 5 mA cm^{-2}. Electrochemical Impedance Spectroscopy (EIS) was done using a sinusoidal signal with a mean voltage of 0 V and amplitude of 10 mV over a frequency range of 0.1 Hz to 100000 Hz. EIS measures the impedance of an SC as a function of frequency.

3. Results and discussion

3.1. Characterization

The X-ray diffraction (XRD) (Rigaku Ultima IV X-ray diffractometer) patterns of Graphite, GO and RGO powders were recorded with a scanning rate of 1° per minute in a 2θ range from 0° to 100° with Cu-Kα radiation (λ = 0.1546 nm, 40 kV and 30 mA) to characterize the carbon-based powders.

XRD patterns obtained for graphite, GO and RGO provide valuable insights into the structural transformations during the synthesis process. As shown in Fig. 1, the XRD pattern of natural graphite powder typically exhibits a sharp peak at 26.48°, corresponding to the (002) crystal plane, indicative of its highly ordered layered structure [23]. Upon oxidation to form GO, the diffraction peak for GO was shifted to $2\theta = 11.38°$ and the intensity of this peak decreases while broadening occurs, suggesting the disruption of the graphite's layered structure and the introduction of oxygen-containing functional groups, such as epoxy, hydroxyl, carbonyl, and carboxyl groups and moisture between layers during chemical oxidation reaction [24]. Subsequent reduction of GO to RGO

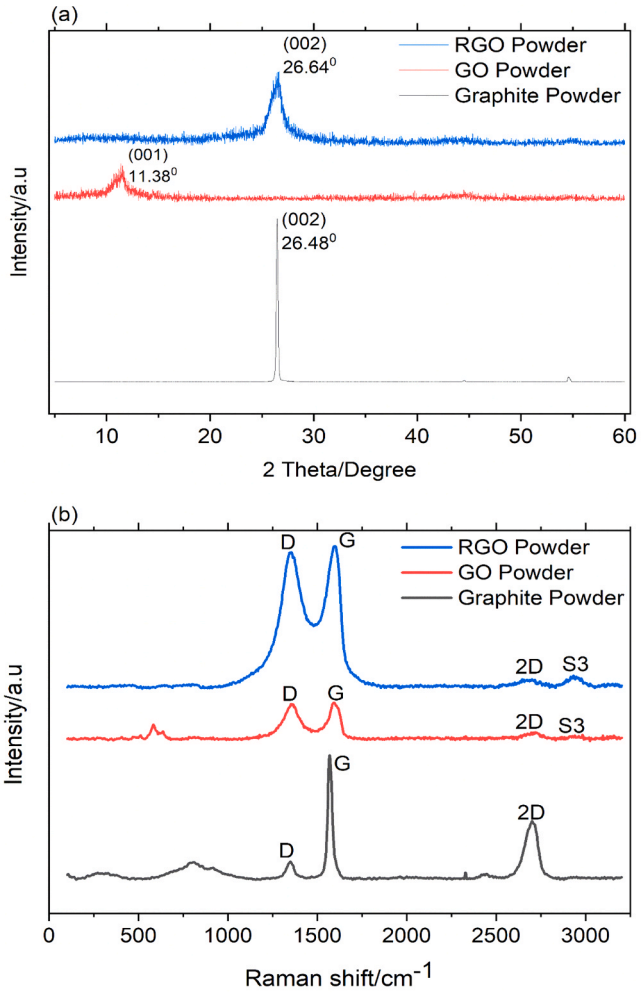

Fig. 1. (a). XRD patterns of graphite, GO and RGO powders (b). Raman spectra of graphite, GO and RGO powders.

leads to a recovery in the intensity of the (002) peak, indicating the restoration of the graphitic structure to some extent. However, the peak remains broadened compared to pristine graphite, indicative of the retention of some disorder and defects introduced during the oxidation process. Additionally, the appearance of new peaks or shifts in peak positions in the XRD patterns of GO and RGO compared to graphite further confirms the structural modifications undergone during the synthesis process [25,26].

We conducted a comprehensive comparative analysis of graphite, GO and RGO powders by determining key structural parameters from XRD patterns. Inter-planar distance (d) refers to the distance between adjacent crystal planes within a material, providing insights into the stacking arrangement and structural integrity. Average crystallite width (D) represents the lateral size of the crystalline domains present in the material, reflecting the degree of crystallinity and the size distribution of individual crystallites. In-plane crystallite size (L) denotes the size of the graphene domains within the material's plane, indicating the extent of lateral growth and structural coherence. The average number of graphene layers per region (n) quantifies the degree of graphene layer stacking, which influences the material's electronic and mechanical properties [27,28]. By analyzing these parameters across graphite, GO and RGO samples, we gained valuable insights into the structural evolution induced by oxidation and reduction processes. This comparative analysis provides critical insights into the synthesis pathways and structural transformation mechanisms of graphene-based materials. This enhances the fundamental understanding of their physicochemical evolution. Such knowledge is essential for the rational design and optimization of graphene derivatives tailored for high-performance applications, particularly in energy storage systems such as SCs, where material properties directly influence electrochemical behavior [29]. Tables 1 and 2

$$d = \frac{n\lambda}{2Sin\theta} \tag{1}$$

$$D = \frac{k\lambda}{\beta Cos\theta} \tag{2}$$

$$L = \frac{1.84\lambda}{\beta Cos\theta} \tag{3}$$

$$n = \frac{D}{d} + 1 = \frac{2k.Tan\theta}{\beta} + 1 \tag{4}$$

where, $\lambda = 0.15406$ nm (wavelength of incident X-ray, $\theta =$ peak position (in radians) $n = 1$ (order of diffraction), $\beta =$ Full peak width of the diffraction peak at half maximum height (FWHM), $K = 0.89$ (that is a constant related to crystallite shape) for spherical crystals with cubic unit cells.

Graphite exhibited a characteristic interplanar distance of approximately 0.33 nm, reflecting its well-defined layered structure. Upon oxidation to form GO, this distance expanded due to the introduction of oxygen-containing functional groups, resulting in a larger interlayer spacing [30]. The average crystallite width of graphite was observed to be relatively large, indicative of its high degree of crystallinity. In contrast, the crystallite width decreased upon oxidation to GO, reflecting a reduction in crystallinity and the formation of smaller crystalline domains [31]. Furthermore, the in-plane crystallite size of graphite was notably extensive, indicating the presence of large graphene domains. However, oxidation led to a reduction in the in-plane crystallite size of GO, reflecting the disruption of the graphene layers into smaller, more disordered domains. Subsequent reduction to RGO resulted in a partial recovery of the inter-planar distance and crystallite size compared to GO, suggesting the restoration of structural order to some extent. However, the values remained slightly lower than those of pristine graphite, indicative of residual defects and disorder [32]. This comparative analysis provides valuable insights into the structural transformations undergone by graphene-based materials during synthesis processes, offering crucial guidance for their tailored design and optimization for SC applications [33].

Table 1
Some physical parameters of graphite, GO and RGO powder obtained from XRD patterns.

Parameter	Graphite Powder	GO Powder	RGO Powder
2θ /degree	26.48	11.38	26.64
d /nm	0.33	0.77	0.33
D /nm	30.14	12.87	1.02
L /nm	66.31	16.44	3.28
n/layers per domain	124	17	8

Table 2
Some physical parameters of graphite, GO and RGO powders calculated from Raman spectroscopy.

Parameter	Graphite Powder	GO Powder	RGO Powder
D band /cm^{-1}	1359.09	1359.10	1355.85
G band /cm^{-1}	1583.10	1597.64	1594.05
I_D/I_G	0.26	0.91	1.10
Lsp^2 /nm	63.11	18.03	14.90
L_D /nm	25.38	13.56	12.34
$nD/\times 10^{11}$ cm^{-2}	0.89	3.12	3.78

Raman spectroscopy plays a pivotal role in characterizing graphite, GO and RGO powders due to its ability to provide detailed structural information at the molecular level. The distinctive Raman spectra of these materials reveal characteristic peaks corresponding to various vibrational modes, such as the G band (associated with sp^2 carbon atoms) and the D band (indicative of structural defects and disorder). The intensity ratio of these bands, known as the I_D/I_G ratio, serves as a quantitative measure of structural disorder and the degree of graphitization. Additionally, Raman spectroscopy enables the identification of additional bands associated with specific functional groups in GO, providing valuable information about the extent of oxidation and the presence of oxygen-containing moieties. Furthermore, the analysis of peak positions and peak shapes in Raman spectra can elucidate the structural evolution of graphene-based materials during synthesis processes [34,35].

We conducted a comparative analysis of graphite, GO and RGO powders using Raman spectroscopy, elucidating distinctive features in their spectra that reflect their structural characteristics. Graphite exhibited a prominent G band at 1583 cm^{-1}, corresponding to the in-plane stretching vibrations of sp^2 bonded carbon atoms, indicative of its highly crystalline nature. Additionally, a relatively weak D band at approximately 1359 cm^{-1}, attributed to the breathing modes of sp^2 carbon atoms in rings and vacancies, was observed, suggesting minimal structural defects [36]. Upon oxidation to GO, the intensity of the D band significantly increased due to the introduction of oxygen-containing functional groups and the disruption of the graphitic structure. This was accompanied by a blue shift and broadening of the G band, reflecting a reduction in the average size of sp^2 domains and an increase in disorder. Moreover, new bands associated with oxygen-containing functional groups emerged in the spectra of GO, providing evidence of functionalization [37]. Subsequent reduction to RGO resulted in a partial restoration of the G band intensity and an increase in the D band intensity compared to GO, indicating a partial recovery of the graphitic structure. Additionally, the emergence of a 2D band at around 2700 cm^{-1} in RGO spectra confirmed the restoration of sp^2 carbon domains. These changes in band intensity, position, and shape observed in Raman spectra provide valuable insights into the structural evolution of graphene-based materials during synthesis processes [38]. Moreover, the intensity ratio of the D band to the G band (I_D/I_G) was focused as a key parameter for comparative analysis. Graphite exhibited a relatively low I_D/I_G ratio, indicative of its high degree of graphitic order and minimal structural defects [26]. Upon

oxidation to GO, this ratio increased significantly due to the introduction of oxygen-containing functional groups, leading to a higher density of structural defects and disorder. The observed increase in the I_D/I_G ratio in GO spectra reflected the disruption of the sp^2 carbon network and the formation of sp^3 hybridized carbon species. Subsequent reduction to RGO resulted in a partial restoration of the graphitic structure, as evidenced by an increase in the I_D/I_G ratio compared to GO. The observed increase indicated a reduction in the density of structural defects and the partial recovery of sp^2 carbon domains. This comparative analysis of the I_D/I_G ratio provides valuable insights into the structural evolution of graphene-based materials during synthesis processes, offering crucial guidance for their tailored design and optimization for SC applications [39].

I_D/I_G ratio is utilized for the estimation of in-plane size of sp^2 domains (Lsp^2), average defect distance (L_D) and defect density (nD, cm^{-2}) using the following equations [27],

$$Lsp^2 = \frac{560 I_G}{E_L^4 I_D} \tag{5}$$

$$L_D^2(nm^2) = 2.4 \times 10^{-9} \lambda_L^4 \frac{I_G}{I_D} \tag{6}$$

$$nD = \frac{2.4 \times 10^{22} I_D}{\lambda_L^4 \quad I_G} \tag{7}$$

where E_L= 2.417 eV and λ_L= 514 nm are the energy and wavelength of the laser source.

We performed a comparative analysis of graphite, GO and RGO powders using Raman spectroscopy, focusing on the determination of key structural parameters: in-plane size of sp^2 domains, average defect distance, and defect density. The in-plane size of sp^2 domains represents the lateral dimension of the crystalline domains within the graphene lattice, indicating the extent of structural ordering [40]. Graphite typically exhibits large in-plane domain sizes due to its highly crystalline nature, whereas the oxidation of graphite to GO leads to a reduction in domain size due to the introduction of structural defects and disruption of the graphene lattice [41]. The average defect distance, on the other hand, quantifies the spacing between structural defects within the graphene lattice, providing insights into the degree of disorder. Higher defect densities and shorter average defect distances are typically observed in GO compared to graphite, reflecting the increased density of functional groups and structural disruptions introduced during oxidation [42].

A high-quality thin films of GO-HNO_3, GO-DMF, RGO-HNO_3 and RGO-DMF were successfully prepared on FTO current collectors and the films were characterized using XRD and Raman measurements to get information about crystal phase and structure. Fig. 2(a) displays the XRD pattern of the prepared four electrodes. The sharp and intense diffraction peaks at 26.36°, 25.35°, 26.19° and 25.86° for GO-HNO_3, GO-DMF, RGO-HNO_3 and RGO-DMF electrodes, respectively. GO (2θ=11.39^0) and RGO (2θ=26.51°) powder were produced and characterized using powder X-ray diffraction as previously described. As shown in Fig. 2(a), the characteristic peaks of RGO are inherited in RGO-HNO_3 and RGO-DMF based electrodes, with weakened intensity in RGO-HNO_3 based electrode and strengthen intensity in RGO-DMF based electrode. This observation may be attributed to the amorphous state of RGO in RGO based electrodes. In addition, there are no some peaks around $2\theta = 11^0$ in XRD patterns of GO-HNO_3 and GO-DMF based electrodes and a weak, broad peak centered around 25^0 were observed. It indicates that the presence of GO did not interfere with the growth of HNO_3 and DMF solvents and change its crystalline structure. In addition, the increased 2θ value can be ascribed to the presence of a small amount of residual oxygen containing functional groups or other structural defects [43]. Raman spectroscopy was used to analyze further the chemical structure of GO-HNO_3, GO-DMF, RGO-HNO_3 and RGO-DMF thin films as

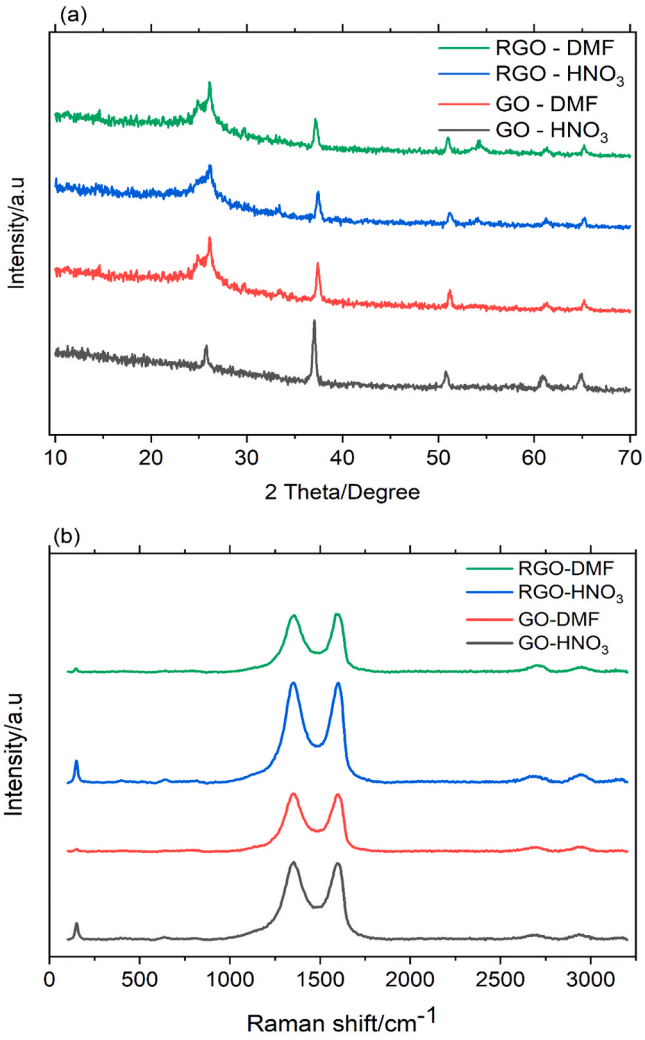

Fig. 2. (a). XRD patterns of GO-HNO_3, GO-DMF, RGO-HNO_3 and RGO-DMF thin films (b). Raman Spectra of GO-HNO_3, GO-DMF, RGO-HNO_3 and RGO-DMF thin films.

shown in Figure. The D peak is related to the defects in sp^2 carbon, while G peak is stretching of C-C sp^2 bonds. The ratio of I_D/I_G gives data about the optical properties of the graphene-based materials. Furthermore, in-plane size of sp^2 domains (Lsp^2), average defect distance (L_D) and defect density (nD) were found using Eq. (5), Eq. (6) and Eq. (7), respectively.

Apparently, the Raman spectrum of GO-HNO_3, GO-DMF, RGO-HNO_3 and RGO-DMF reveal well marked D-band and G-band located at around 1300 cm^{-1} and 1550 cm^{-1} which corresponds to the structural irregular defects as shown Table 3. The in-plane size of sp^2 domains of GO-HNO_3 and GO-DMF electrodes slightly decrease relative to GO powder. The in-plane size of sp^2 domains of RGO-HNO_3 and RGO-DMF electrodes slightly increase relative to RGO powder. There is no any noticeable change in average defect distance and defect density.

Scanning Electron Microscopy (SEM) plays a pivotal role in assessing the performance of SC electrode materials due to its ability to provide high-resolution images at nanoscale levels. In the context of thin films of electrode material for SCs, SEM enables us to analyze the morphology, surface roughness, and structural integrity of the films. These factors are crucial determinants of the electrode's specific surface area, porosity, and interfacial properties, which directly influence the electrochemical performance of the SCs [5]. Additionally, SEM can reveal defects, cracks, and agglomerations within the electrode material, offering insights into its mechanical stability and long-term durability [44].

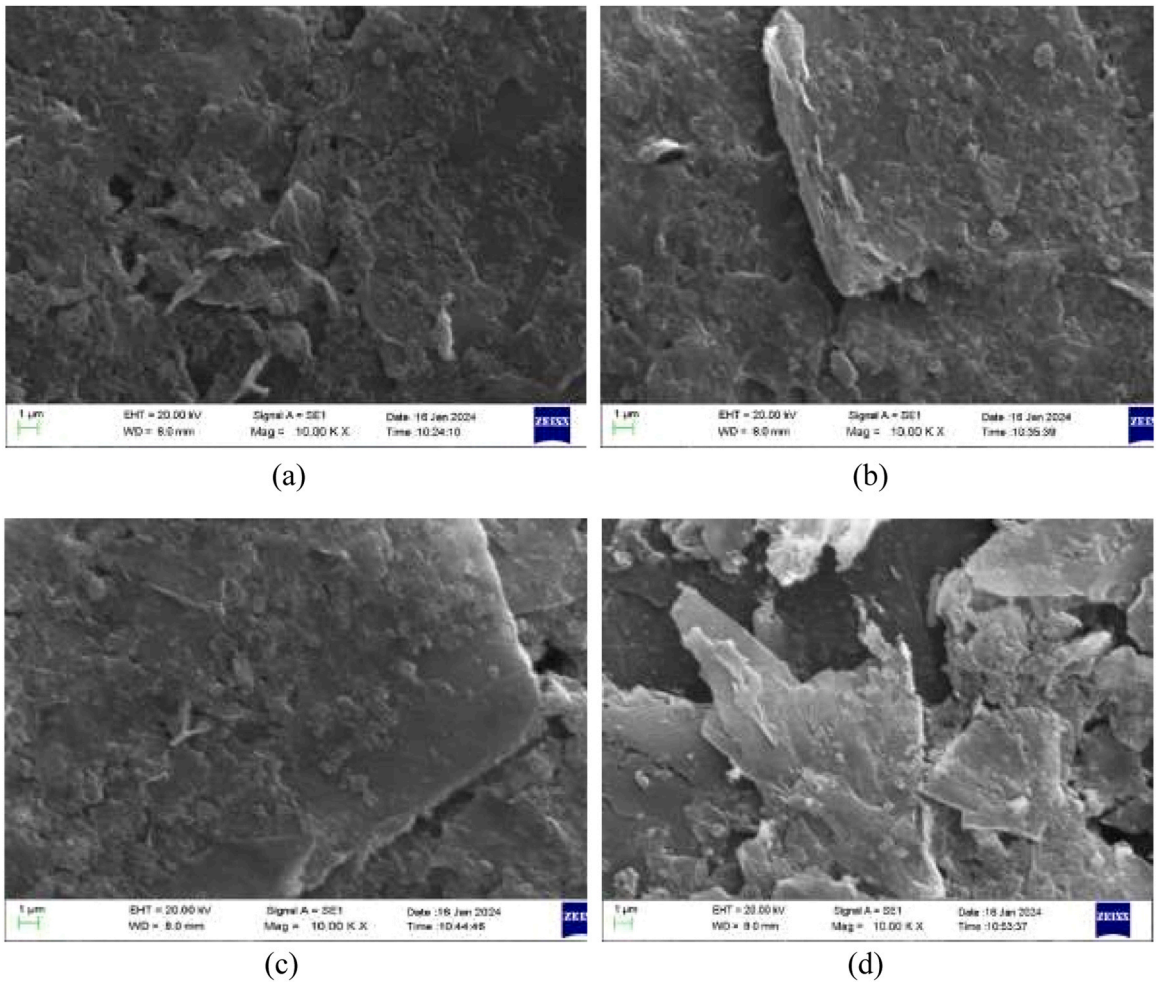

Fig. 3. SEM images of (a) GO-HNO_3 based thin film (b) GO-DMF based thin film (c). RGO-HNO_3 based thin film (d). RGO-DMF based thin films.

Table 3
Some physical parameters of thin films obtained from Raman spectroscopy.

Thin film	D – band /cm^{-1}	G – band /cm^{-1}	I_D/I_G ratio	Lsp^2 /nm	L_D /nm	nD /$\times 10^{11}$ cm^{-2}
GO-HNO_3	1353.96	1597.64	1.02	16.08	12.81	3.50
GO-DMF	1353.03	1599.28	1.01	16.24	12.87	3.47
RGO-HNO_3	1352.52	1600.54	0.99	16.57	13.00	3.40
RGO-DMF	1355.16	1590.02	0.97	16.91	13.14	3.33

The SEM images of the four thin films synthesized for SC applications reveal distinctive morphological features that can significantly impact their electrochemical performance. Firstly, the GO film prepared with nitric acid solvent and TiO_2 binder exhibits a relatively smooth surface with dispersed TiO_2 particles, indicating good film formation and uniform distribution of the binder material [45]. In contrast, the GO film synthesized using DMF solvent displays a more porous structure with fewer visible TiO_2 particles, suggesting differences in film morphology and binder distribution. Moving to RGO films, those fabricated with nitric acid solvent and TiO_2 binder exhibit a somewhat rougher surface compared to their GO counterparts, likely due to the reduction process that restores graphene-like properties and enhances surface roughness [46]. Additionally, the presence of TiO_2 particles appears more pronounced and uniformly dispersed within the RGO matrix, indicating effective binder integration and potential enhancement of electrochemical properties. Conversely, the RGO film synthesized with DMF solvent and TiO_2 binder exhibits a porous and interconnected network structure, possibly due to the solvent's ability to facilitate better dispersion and intercalation of TiO_2 particles within the RGO matrix. This structure could potentially offer improved electrolyte accessibility and ion diffusion kinetics, leading to enhanced charge storage capabilities [47]. Overall, the SEM analysis suggests that the choice of solvent and binder, along with the graphene derivative used, has a significant impact on the morphology and microstructure of the thin films, ultimately influencing their electrochemical performance in SC applications.

3.2. Electrochemical analysis

All four electrodes (GO-HNO_3, GO-DMF, RGO-HNO_3 and RGO-DMF based electrodes) were first analyzed for their electrochemical performance using cyclic voltammetry (CV) curves. CV responses of the electrodes were measured in the 0 V to 1 V potential window. The potential window was scanned from the anodic to cathode voltage direction at different scan rates between 2 mVs^{-1} and 100 mVs^{-1}.

An ideal SC would show a perfectly square shape when undergoing a

CV analysis. In Fig. 4, we show CVs at scan rates of 2, 5, 10, 20, 50 and 100 mVs^{-1} for all four SCs built using graphene as electrodes and 2 M H_2SO_4 acid as electrolyte. However, due to electrolyte ion diffusion and resistance during CV analysis, pseudo-rectangular shapes were observed without distinct redox peaks [48]. Whether at a relatively low scanning rate or high, all the curves exhibited symmetry and very approximate rectangular shape, suggesting that the good charge propagation within the electrode which stores energy using the adsorption of both anions and cations. However, with increasing scan rates the rectangular shape deforms which can be due to charge transport limitations [49]. Calculated specific capasitance (C_{sp}) values of four SCs are given in Table 4 as a function of the potential scan rate. Table 4 demonstrates that at the lower scan rates, all the electrodes show the higher C_{sp}. It decreases significantly with the increment of scan rate may be due to the relaxation of charge transport in particular in the pores, rapid motion of massive ions which results in poor accommodation of ions inside the pores of graphene and consequence of mobility of massive electrolyte ions. At high scan rates, the ions get insufficient time to diffuse into the pores of graphene which results in a simple polarization followed by the accumulation of charges at the surface of the electrode [50]. However, the fall in specific capacitance of GO – HNO_3 and GO – DMF based SCs between 2 mV s^{-1} and 5 mV s^{-1} not too rapid as shown in Figure 04 (b). This may be attributed to the highly porous nature of the surface of electrolyte with well-connected pores which facilitates the electrolyte ions to find a shortest directional path [51]. At high scan rates, the ions get insufficient time to diffuse into the pores of graphene which results in a simple polarization followed by the accumulation of charges at the surface of the electrode. The highest C_{sp} value of 146 F g^{-1} was observed for the RGO – DMF electrode among these four electrodes [52]. Fig. 5

The specific capacitance using the CV curves was reported by integrating over the full CV curve to determine the average value [53],

$$C_{sp} = 4\frac{\int I.dt}{V \times S \times M_{ac}} \tag{8}$$

Table 4
Specific capacitance values at different scan rates for different electrode materials.

Scan Rates /mV s^{-1}	Specific Capacitance /F g^{-1}			
	GO-HNO_3	GO-DMF	RGO-HNO_3	RGO-DMF
2	65.79	131.03	125.59	146.03
5	63.24	128.13	113.05	118.70
10	55.78	112.14	98.86	91.99
20	43.29	78.70	70.95	65.54
50	24.72	39.95	48.03	37.77
100	13.28	20.51	19.46	22.75

where,

I = current, V = voltage range, S = scan rate, M_{ac} = electrochemically active mass of the cell.

The term $\int I\,dt$ was calculated by integrating the area enclosed by the CV curves.

The comparative analysis of C_{sp} with scan rate reveals intriguing insights into the electrochemical performance of GO and RGO based SCs. Across all materials and synthesis methods (GO-HNO_3, GODMF, RGO-HNO_3, and RGO-DMF), there is a noticeable trend of decreasing specific capacitance with increasing scan rates. This phenomenon is attributed to the limitations imposed by faster scan rates, which result in reduced ion diffusion kinetics and limited accessibility of active sites on the electrode surface [54]. However, it is noteworthy that specific capacitance values for GO-DMF and RGO-DMF are consistently higher compared to their counterparts synthesized using HNO_3 as the solvent. This discrepancy underscores the significant impact of solvent choice on the electrochemical properties of graphene-based materials, with DMF facilitating the formation of electrodes with higher capacitance. Furthermore, the specific capacitance values obtained at lower scan rates (2 and 5 mV s^{-1}) are significantly higher compared to those at higher scan rates (50 and 100 mV s^{-1}), emphasizing the importance of optimizing scan

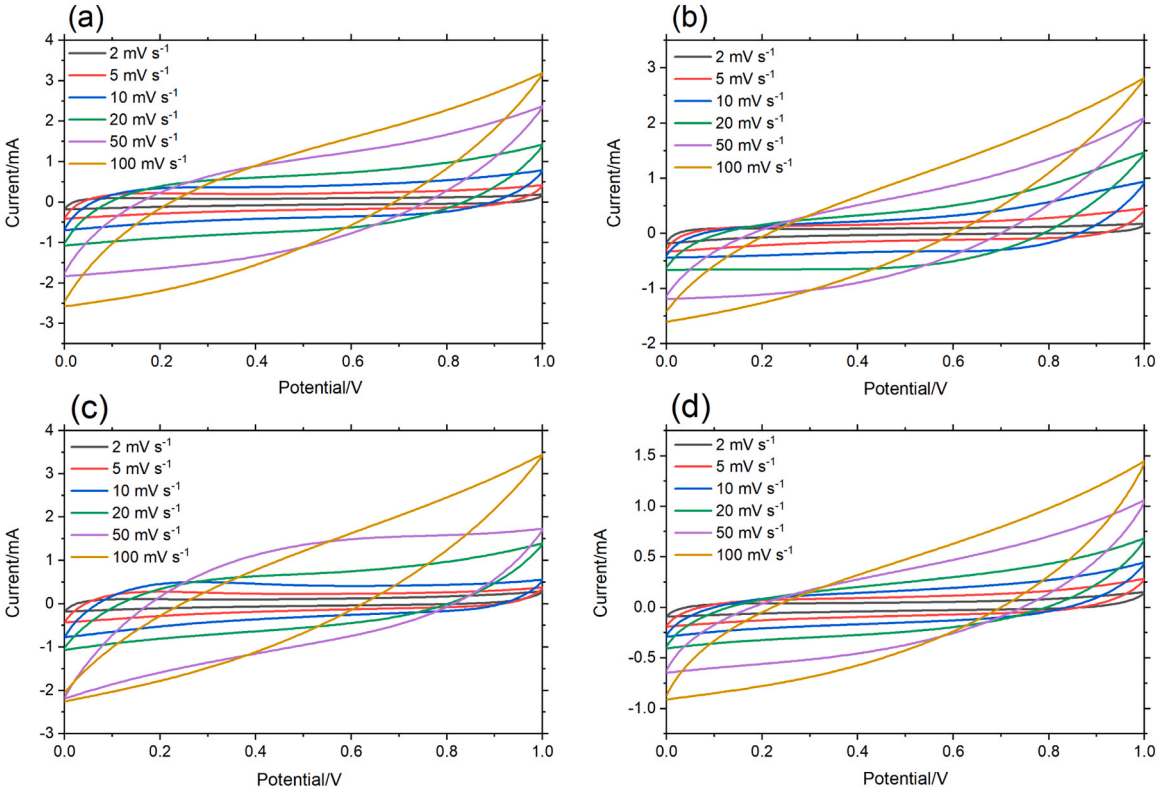

Fig. 4. Cyclic voltammetry curves for different scan rates (a). GO-HNO_3 based SC (b). GO-DMF based SC (c). RGO-HNO_3 based SC (d). RGO-DMF based SC with 2 M H_2SO_4 acidic electrolyte.

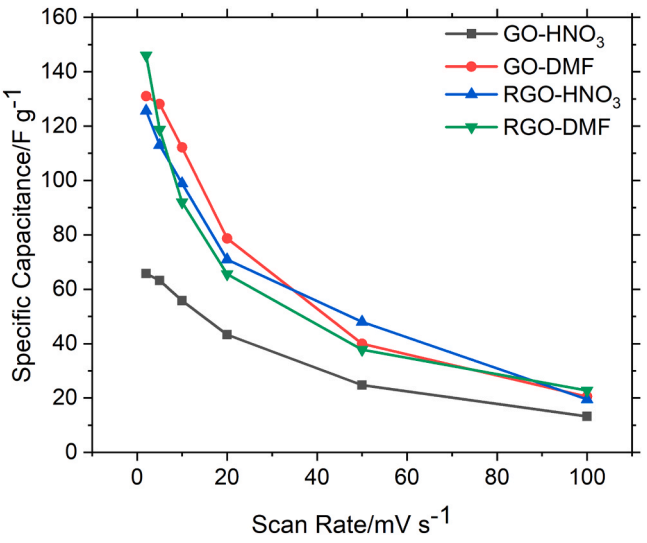

Fig. 5. Specific capacitance as a function of scan rate.

rate for achieving superior electrochemical performance in SCs. This comparative analysis underscores the critical role of synthesis methods and scan rates in tailoring the specific capacitance of graphene-based SCs, providing valuable insights for the design and optimization of high-performance energy storage devices.

The gravimetric energy density (E_g) and gravimetric power density (P_g) are key parameters that determine the performance of SCs. E_g refers to the amount of energy that a SC can store per unit mass. P_g is a measure of how quickly SC can deliver energy [48]. The parametric relationship of the E_g and related P_g provides a greater insight into the device functional aspects of GO and RGO based electrodes with HNO_3 and DMF solvents separately with 2 M H_2SO_4 electrolyte. The values of E_g and P_g of the four cells (GO-HNO_3, GO-DMF, RGO-HNO_3 and RGO-DMF) were calculated by studying the Galvanic charge-discharge (GCD) characteristics using the combined active electrode mass (M_{ac}) at various current loads in the range 0.5 mA cm^{-2} to 5 mA cm^{-2}. The values of E_g and P_g were calculated from [55],

$$C = \frac{4I}{M_{ac}\ \frac{\Delta V}{\Delta t}} \tag{9}$$

$$E_g = \frac{1}{2}CV^2 \tag{10}$$

$$P_g = \frac{E_g}{t} \tag{11}$$

where, C = Gravimetric capacitance which was evaluated from the slope of discharge curve

I = Current density, V = Potential component of discharge slope, t = Time component of discharge slope

According to the GCD curves in Fig. 6(a) and Eqs. (9), (10) and (11), we have calculated the values of E_g and P_g of four cells and presented them in Table 5. As a result, a maximum E_g value of 21.58 Wh kg^{-1} can be achieved with P_g value 1.21 kW kg^{-1} at constant current density 0.5 mA cm^{-2} for GO-DMF electrode-based cell and a maximum P_g value is 81.5 kW kg^{-1} with E_g value 0.96 Wh kg^{-1} at constant current 5 m A cm^{-2} for RGO-DMF based electrode. This data shows that the electrochemical performance of DMF is better than HNO_3 as a solvent. Fig. 6(a) shows the symmetric nature of GCD curves at 0.5 mA cm^{-2} current density, which clearly matches CV curves as shown in Fig. 4. We could clearly identify the fabricated symmetric SCs can be operated up to wider potential window 1.0 V without any evolution occurred. Further, the E_g of the electrode material is indicated through the discharging period in the GCD curves where a longer discharging time indicates a better energy density value. Interestingly, as shown in Fig. 6(a), HNO_3 solvent based stacked devices were recorded a longer discharging time compared to DMF solvent based devices. But the E_g performance of DMF solvent based devices has an advantage over the HNO_3 solvent based devices which is approximately 2 times higher than that of lower one as listed in Table 5. It is evident that the swiftness of the ion transport and pervasive ion access for built-up of the electrical double layer at the graphene platelet interface with acidic liquid electrolyte [56]. The structure of electrical double layer and thus performance of SC could be affected by the charge and size of ions [57]. Consequently, as shown in Fig. 6(a), the typical GCD curves at 0.5 mA cm^{-2} current are linear

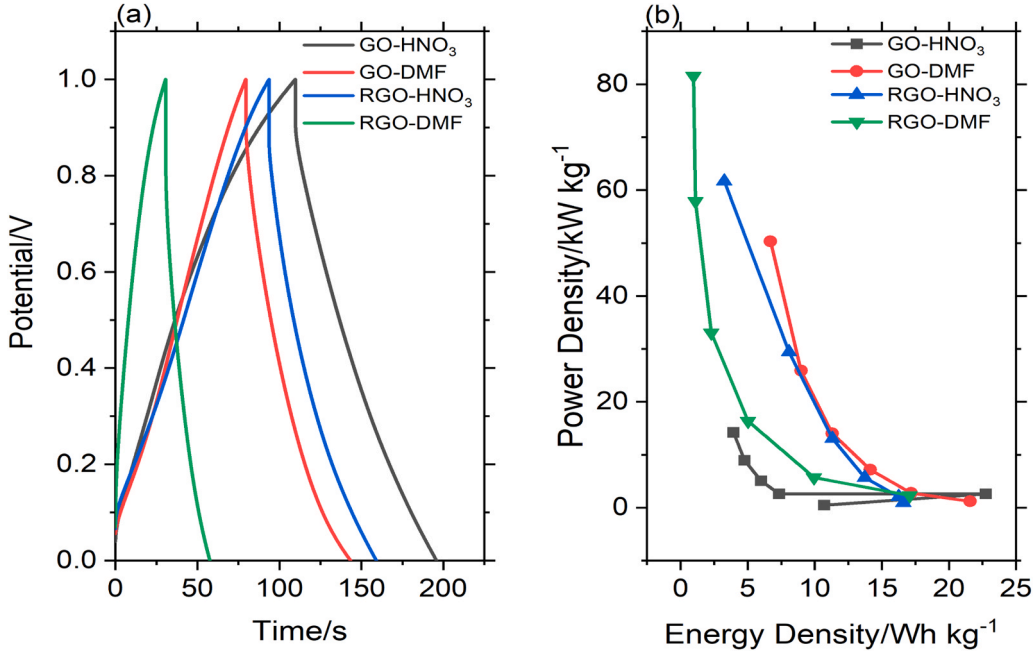

Fig. 6. (a). GCD curves for four electrodes GO – HNO_3, GO – DMF, RGO – HNO_3 and RGO-DMF at the current density 0.5 mA cm^{-2} (b). Variation of P_g as a function of E_g.

Table 5
E_g values and P_g values for different electrode materials with different constant current densities.

Current (mA cm^{-2})	GO – HNO_3		GO - DMF		RGO – HNO_3		RGO - DMF	
	Eg /Wh kg^{-1}	P_g /kW kg^{-1}	E_g /Wh kg^{-1}	P_g /kW kg^{-1}	E_g /Wh kg^{-1}	P_g /kW kg^{-1}	E_g /Wh kg^{-1}	P_g /kW kg^{-1}
0.5	10.69	0.44	21.58	1.21	16.60	0.91	17.07	2.27
1.0	22.76	2.62	17.18	2.78	16.26	2.09	9.94	5.68
2.0	7.34	2.59	14.14	7.16	13.73	5.70	5.03	16.33
3.0	5.99	5.07	11.30	14.03	11.32	13.06	2.29	33.07
4.0	4.76	8.93	8.98	25.87	8.09	29.42	1.12	57.86
5.0	3.94	14.19	6.70	50.30	3.25	61.66	0.96	81.55

across the entire charging and discharging time for all four cells reaffirming the capacitive nature arising from the electrical double layer in the graphene-based SC device [58]. In terms of advancement made on the energy density increasing for SCs, another important work worth mentioning is the porous yet densely packed graphene oxide and reduced graphene oxide electrodes with high ion accessible specific surface area and low ion transport resistance, efficient electron and ion transport pathways, high packing density and pores can also speed-up the ion transport across the 2D plane of the graphene [59]. Furthermore, the pores in graphene sheets are large enough to function as the ion diffusion shortcuts between different layers of graphene to greatly accelerate the ion transportation across the entire film [57].

The favorable variation of the E_g with increasing P_g as shown in the Fig. 6(b) reminisces the behavior of an electrical double layer SC power device exemplified by the tendency towards the reduction in E_g as P_g increases when higher current loads are applied. The decrease in the E_g of GO-HNO_3 is not as significant at the corresponding increase in the P_g which suggests high power functionality of the acidic electrolyte in the GO based SC. In the case of the other three cells, the decrement of E_g is slightly aggravated. As demonstrated in Fig. 6, RGO based SCs exhibited high energy densities relative to GO based SCs. This result can certainly be attributed to the reduction of graphene oxide. GO consists of graphene sheets with oxygen containing functional groups while the reduction process involves removing a substantial portion of oxygen containing functional groups from GO. The reduction of GO typically leads to the restoration of some π-conjugated regions and improved electrical conductivity [60]. The improvement of electrical conductivity of GO is directly connected with the values of E_g. From the values of E_g of GO-DMF and RGO-DMF based SCs, we could obtain that the E_g values of GO-DMF based SC were higher than RGO-DMF based SC. This suggests that the effect of the solvent is more important than the effect of reduction of GO. In summary, there is a trade-off between E_g and P_g in GO and RGO based SCs, which are designed to balance these two parameters effectively, offering a good compromise between energy storage capacity and the ability to deliver energy rapidly [61]. Table 6

Our Experimental results demonstrated that the highest C_{sp} achieved was 146.03 F g^{-1} at 2 mV s^{-1} with RGO-DMF electrode. Comparatively, CNT-Graphene films and GF/PANI in 1 M H_2SO_4 reported C_{sp} values of 140 F g^{-1} and 311.3 F g^{-1}, respectively, indicating that while our C_{sp} values are competitive, there is room for improvement. Our E_g reached up to 21.58 Wh kg^{-1} and power P_g up to 81,555.26 W kg^{-1}, particularly excelling in P_g compared to other materials such as GF/PANI (539.9 W kg^{-1}) and PANI/Vertical Graphene/Ti multilayer composites (383 W kg^{-1}). This positions our RGO-based SC as highly effective for applications requiring high power output.

The Nyquist plot (NP) serves as a critical tool in assessing the performance of SCs by providing valuable information about their electrochemical impedance characteristics. This plot, typically obtained through electrochemical impedance spectroscopy (EIS), depicts the complex impedance of the SC as a function of frequency [74]. The shape and features of the NP offer insights into various electrochemical processes, such as charge transfer resistance, double-layer capacitance, and Warburg impedance. Analyzing the NP enables us to evaluate the effectiveness of electrode materials, electrolytes, and device configurations in terms of their electrical conductivity, ion diffusion kinetics, and overall impedance matching [75]. Fig. 7 shows the in the frequency range between 0.1 Hz to 100000 Hz. It can be seen that both the spectra show common features: a small semi-circle at the higher frequency, a second larger capacitive loop at the lower frequency and a straight line in the middle frequency part related to the diffusion [76]. The internal resistance R_s was obtained from the intercept of the semicircle with the real axis (Z') at high frequencies was used to evaluate the resistance associated with the transport within the porous structures of the electroactive materials. On the other hand, the semicircle along Z' at the

Table 6
C_{sp}, E_g, P_g and cycling stability values of RGO based SCs with different acidic electrolytes along with reference.

Electrode Material	Electrolyte	C_{sp} (F g^{-1})	E_g (Wh kg^{-1})	P_g (W kg^{-1})	Cycling Stability	References
RGO/Fe_2O_3	0.5 M H_2SO_4	81	-	-	-	[62]
CNT-Graphene films	1 M H_2SO_4	140	-	5100	96.15 % after 2000 cycles	[63]
GF/PANI	1 M H_2SO_4	311.3	66.3	539.9	-	[64]
PANI/Vertical Graphene/Ti multilayer electrode composite	0.5 M H_2SO_4	535.7	26.1	383	86 % after 10000 cycles	[65]
Electro-chemically tailored 3D RGO	Polyvinyl alcohol/H_3PO_4 gel	81	11.25	5000	94.5 % after 5000 cycles	[66]
Folded graphene paper	1 M H_2SO_4	172	-	-	99 % after 5000 cycles	[67]
Cellulose – graphene paper	1 M H_2SO_4	120	-	-	99 % after 5000 cycles	[68]
PANI-graphene Components	1 M H_2SO_4	233	-	-	-	[69]
PANI-graphene nanofiber component	1 M H_2SO_4	210	-	-	79 % after 800 cycles	[70]
3D-N and B co-doped graphene nanosheets	1 M H_2SO_4	239	8.7	1650	100 % after 1000 cycles	[71]
RGO/Carbon black	PVA/H_2SO_4	79	-	-	-	[72]
Multilayer RGO	PVA/H_3PO_4	247.3	-	-	-	[73]

Abbreviations for Table 06,
PANI – Polyaniline
CNT – Carbon nanotubes
IL – Ionic liquids
CMG – Chemically modified graphene
PVA – Polyvinyl alcohol
GF – Graphene foam

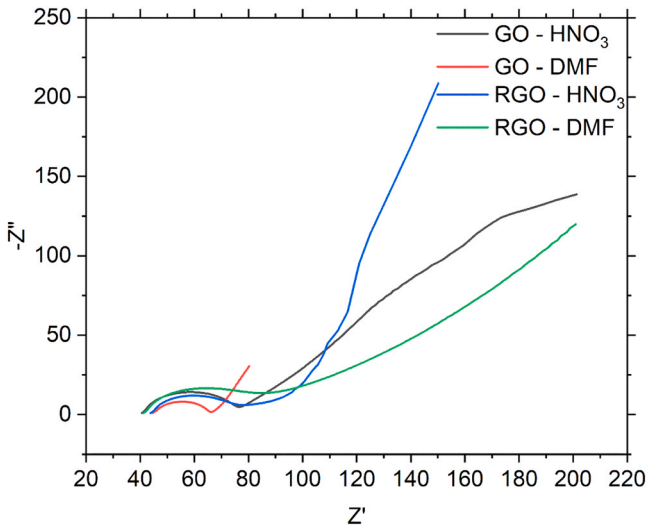

Fig. 7. Nyquist Plots of the electrochemical impedance spectroscopy of four SCs.

higher frequency range was due to the ionic charge transfer resistance (R_{ct}) at the electrode and electrolyte interface [77]. As shown in the Fig. 7, these low R_s and R_{ct} resistances should be attributed to the porosity of the systems, which favors the access and escape of the electrolyte ions in to the electroactive materials, enhanced electrical conductivity and fast electrochemical reaction at the electrode-electrolyte interface of the material [78]. The largest semi-circle has been observed for GO-DMF based electrodes with the addition of DMF in H_2SO_4 acidic electrolyte which infers high ionic resistance. Consequently, in all other cases, there was small ~ 45° inclined line at middle frequency which is known as diffusive or Warburg resistance [79]. Furthermore, the straight lines of the GO-DMF and RGO-DMF based cells indicated in the low frequency region which appeared more perpendicular towards the *Z'* axis, indicating a more ideal capacitance behavior. All these cells with low R_s/R_{ct} show a much higher specific capacitance compared to those with a lower resistance as illustrated in Fig. 3 [80].

The cyclic stability of RGO in DMF solvent with 2 M sulfuric acid electrolyte is determined by sequential CV curves for 1000 cycles at the scan rate 100 mV s^{-1} as shown in Fig. 8. In the case of SC was charged from 0 V to 1 V. The specific capacitance increases till the 200th and the maximum value is 1.1 times the initial one. The increased trend is similar to that of functionalized graphene. The peculiar phenomenon may arise whether from the reduction of partially unstable oxygen functional groups in RGO or the exertion of pseudocapacitance in a slow kinetics course. After 200 cycles, an initial capacitance fading by 22 % until 400th cycle due to decreased pseudocapacitance resulting from stable functional groups in the electrochemical system. After 400 cycles, a gradual increment of the C_{sp} was observed to 1000 cycles which is caused by electrolyte ion conductivity and an electronic resistance of RGO-DMF based electrode. The final retention reaches 91.7 % after 1000 cycles.

Although detailed post-mortem characterization such as SEM or Raman analysis was not conducted, visual inspection of the electrode surfaces after 1000 CV cycles displayed no apparent physical damage, delamination, or discoloration. The undistorted morphology and steady electrochemical performance throughout the cycling test indicate good structural stability of the electrode films. Future research will be focused on advanced post - cycling characterizations in order to further confirm the long - term durability of the material system.

For contextual testing, the electrochemical performance of the RGO - DMF electrode (146 F g^{-1} at 2 mV s^{-1} and 81.55 kW kg^{-1} at 5 mA cm^{-2}) were compared against common benchmark materials such as activated carbon (AC), carbon nanotubes (CNTs), and commercial graphene. AC electrodes show a C_{sp} of 100–120 F g^{-1} in aqueous electrolytes under similar testing environments, while CNTs and commercial graphene fall in the 100–180 F g^{-1} range depending on the morphology and electrolyte compatibility. Our RGO-DMF electrode not only meets but exceeds these reference values in both C_{sp} and P_g, illustrating the effectiveness of solvent choice and GO reduction approach. This comparison demonstrates the competitive performance of our material system, positioning it as a viable alternative for high - power SC applications.

4. Conclusion

In this paper, we analyzed and presented how graphene-based electrode materials and solvents influence the specific capacitance, energy density, power density and impedance of SCs. According to the results obtained, RGO electrodes-based SCs exhibit superior performance compared to that of GO – electrodes based CSs. In particular, our results show that RGO – DMF electrode has the highest specific capacitance and power density of 146 F g^{-1} and 81.55 kW kg^{-1}, respectively. The maximum value of E_g of 21.58 Wh kg^{-1} was observed at 0.5 mA cm^{-2} for GO – DMF electrode and the maximum value of P_g was exhibited as 81.55 kW kg^{-1} at 5 mA cm^{-2} for RGO – DMF electrodes. According to our findings, DMF is a better solvent to prepare GO and RGO based electrodes**.** In addition, comparison with established carbon-based electrode benchmarks validates that the electrochemical performance of the RGO - DMF electrodes is competitive, particularly in terms

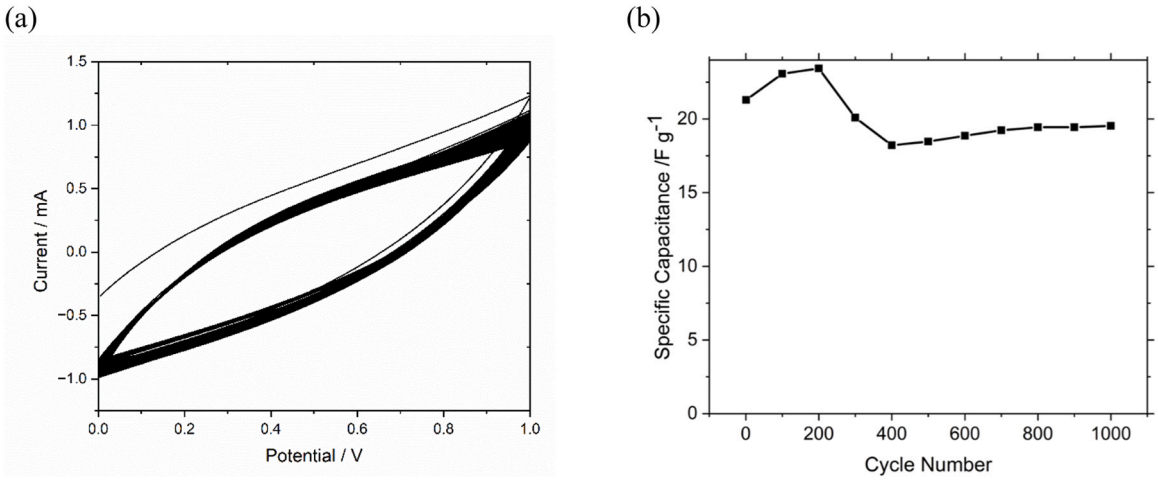

Fig. 8. (a). CV curves for 1000 cycles RGO-DMF SC with 2 M H_2SO_4 (b). Cyclic stability of RGO-DMF based SC at scan rate 100 mV s^{-1}.

of C_{sp} and P_g. Visual inspection after prolonged cycling revealed no apparent physical damage or film degradation, indicating promising structural stability. These observations collectively support the practical applicability and scalability of the developed GO and RGO - based electrodes for future SC device development.

Declaration of Competing Interest

The authors declare that they have no known competing financial interests or personal relationships that could have appeared to influence the work reported in this paper.

References

[1] S. Sharma, S. Agarwal, A. Jain, Significance of hydrogen as economic and environmentally friendly fuel, Energies 14 (21) (2021), https://doi.org/10.3390/en14217389.

[2] Z. Cabrane, D. Batool, J. Kim, K. Yoo, Design and simulation studies of battery-supercapacitor hybrid energy storage system for improved performances of traction system of solar vehicle, J. Energy Storage 32 (September) (2020) 101943, https://doi.org/10.1016/j.est.2020.101943.

[3] M. Uno, K. Tanaka, Unregulated interface converter based on cascaded switched capacitor converters for supercapacitors in alternative battery applications, Proc. Int. Conf. Power Electron. Drive Syst. (December) (2011) 579–586, https://doi.org/10.1109/PEDS.2011.6147308.

[4 S. Majid, A.S.G. Ali, W.Q. Cao, R. Reza, Q. Ge, Biomass-derived porous carbons as supercapacitor electrodes-A review, Xinxing, Tan. Cailiao/N. Carbon Mater. 36 (3) (2021) 546–572, https://doi.org/10.1016/S1872-5805(21)60038-0.

[5] X.Y. Luo, Y. Chen, Y. Mo, A review of charge storage in porous carbon-based supercapacitors, Xinxing Tan. Cailiao/N. Carbon Mater. 36 (1) (2021) 49–68, https://doi.org/10.1016/S1872-5805(21)60004-5.

[6] S. Thakur, N. Karak, Green reduction of graphene oxide by aqueous phytoextracts, Carbon N. Y. 50 (14) (2012) 5331–5339, https://doi.org/10.1016/j.carbon.2012.07.023.

[7] S.K. Pal, Versatile photoluminescence from graphene and its derivatives, Carbon N. Y. 88 (February) (2015) 86–112, https://doi.org/10.1016/j.carbon.2015.02.035.

[8] B. Ahmed, C. Xia, H.N. Alshareef, Electrode surface engineering by atomic layer deposition: A promising pathway toward better energy storage, Nano Today 11 (2) (2016) 250–271, https://doi.org/10.1016/j.nantod.2016.04.004.

[9] X. Du, S. Wang, Y. Liu, M. Lu, K. Wu, M. Lu, Self-assembly of free-standing hybrid film based on graphene and zinc oxide nanoflakes for high-performance supercapacitors, J. Solid State Chem. 277 (May) (2019) 441–447, https://doi.org/10.1016/j.jssc.2019.06.003.

[10] Y.R. Chen, K.F. Chiu, H.C. Lin, C.Y. Hsieh, C.B. Tsai, B.T.T. Chu, The effect of dispersion status with functionalized graphenes for electric double-layer capacitors, Mater. Sci. Eng. B 190 (2014) 59–65, https://doi.org/10.1016/j.mseb.2014.09.011.

[11] R. Liu, L. Chen, S. Yao, Y. Shen, Pore-scale study of capacitive charging and desalination process in porous electrodes and effects of porous structures, J. Mol. Liq. 332 (2021) 115863, https://doi.org/10.1016/j.molliq.2021.115863.

[12] B.M. Gunasekaran, S. Manoj, G.K. Rajendran, et al., Covalently anchored benzimidazole-reduced graphene oxide as efficient electrochemical supercapacitor electrode material, J. Mater. Sci Mater. Electron 34 (2023) 2280, https://doi.org/10.1007/s10854-023-11679-x.

[13] F. Chen, et al., Ethanol-assisted graphene oxide-based thin film formation at pentane-water interface, Langmuir 27 (15) (2011) 9174–9181, https://doi.org/10.1021/la201230k.

[14] S. Mohammadzadeh, H.R. Zare, H. Khoshro, K. Ghobadi, A. Benvidi, The electrochemical behavior of 4-nitrobenzyl bromide and its catalytic activity for reduction of CO2 in the acetonitrile solvent at the Cu/Pd/rGO/GCE surface, Electrochim. Acta 352 (2020) 136483, https://doi.org/10.1016/j.electacta.2020.136483.

[15] K. Min, et al., A facile route to fabricate stable reduced graphene oxide dispersions in various media and their transparent conductive thin films, J. Colloid Interface Sci. 383 (1) (2012) 36–42, https://doi.org/10.1016/j.jcis.2012.06.021.

[16] I.M. Afanasov, et al., Graphite structural transformations during intercalation by HNO3 and exfoliation, Carbon N. Y. 48 (6) (2010) 1862–1865, https://doi.org/10.1016/j.carbon.2010.01.055.

[17] D. Mishra, M.K. Jangid, S. Chhangani, P. Gandharapu, M.J.N.V. Prasad, A. Mukhopadhyay, Lattice Distortion of Current Collector upon Supporting Dimensional Changes of Electrode-Active Materials in Alkali-Metal-Ion Batteries, Energy Fuels 34 (6) (2020) 7763–7769, https://doi.org/10.1021/acs.energyfuels.0c01516.

[18] Z. Yang, et al., Three-Dimensional Photonic Crystal Fluorinated Tin Oxide (FTO) Electrodes: Synthesis and Optical and Electrical Properties, ACS Appl. Mater. Interfaces 3 (4) (2011) 1101–1108, https://doi.org/10.1021/am1012408.

[19] K. Mahankali, N.K. Thangavel, Y. Ding, S.K. Putatunda, L.M.R. Arava, Interfacial behavior of water-in-salt electrolytes at porous electrodes and its effect on supercapacitor performance, Electrochim. Acta 326 (2019) 134989, https://doi.org/10.1016/j.electacta.2019.134989.

[20] Y. Sun, et al., Salty Ice Electrolyte with Superior Ionic Conductivity Towards Low-Temperature Aqueous Zinc Ion Hybrid Capacitors, Adv. Funct. Mater. 31 (28) (2021) 1–10, https://doi.org/10.1002/adfm.202101277.

[21] S. Srinivasan, S. Muthiah, G.K. Rajendran, J.R. Sivanesan, N. Nesakumar, B. M. Gunasekaran, Covalently incorporated heterocyclic benzotriazole-reduced graphene oxide as a high-performance electrochemical supercapacitor electrode, Mater. Sci. Eng. B 301 (2024) 117128, https://doi.org/10.1016/j.mseb.2023.117128.

[22] G.B. Mahendran, S.J. Ramalingam, J.B.B. Rayappan, et al., Green preparation of reduced graphene oxide by *Bougainvillea glabra* flower extract and sensing application, J. Mater. Sci Mater. Electron 31 (2020) 14345–14356, https://doi.org/10.1007/s10854-020-03994-4.

[23] S. Zhang, et al., Structural order evaluation and structural evolution of coal derived natural graphite during graphitization, Carbon N. Y. 157 (2020) 714–723, https://doi.org/10.1016/j.carbon.2019.10.104.

[24] M.F.R. Hanifah, et al., Facile synthesis of highly favorable graphene oxide: Effect of oxidation degree on the structural, morphological, thermal and electrochemical properties, Materialia 6 (May) (2019) 100344, https://doi.org/10.1016/j.mtla.2019.100344.

[25] A. Thakur, S. Kumar, V.S. Rangra, Synthesis of reduced graphene oxide (rGO) via chemical reduction, AIP Conf. Proc. 1661 (2015) (2015), https://doi.org/10.1063/1.4915423.

[26] M.C. Ramakrishnan, R.R. Thangavelu, Synthesis and characterization of reduced graphene oxide, Adv. Mater. Res. 678 (2013) 56–60, https://doi.org/10.4028/www.scientific.net/AMR.678.56.

[27] A. Kaushal, S.K. Dhawan, V. Singh, Determination of crystallite size, number of graphene layers and defect density of graphene oxide (GO) and reduced graphene oxide (RGO), AIP Conf. Proc. 2115 (July) (2019) 1–5, https://doi.org/10.1063/1.5112945.

[28] H. Rennhofer, D. Loidl, S. Puchegger, H. Peterlik, Structural development of PAN-based carbon fibers studied by in situ X-ray scattering at high temperatures under load, Carbon N. Y. 48 (4) (2010) 964–971, https://doi.org/10.1016/j.carbon.2009.11.012.

[29] G.B. Mahendran, S.J. Ramalingam, J.B.B. Rayappan, M.B. Gumpu, R. Ganesh Kumar, M. Lakshmanakumar, N. Nesakumar, Amperometric detection of mercury ions using piperazine-functionalized reduced graphene oxide as an efficient sensing platform, e202103601, Chem. Sel. 7 (12) (Feb. 2022), https://doi.org/10.1002/slct.202103601. e202103601.

[30] H. Yu, et al., The roles of oxygen-containing functional groups in modulating water purification performance of graphene oxide-based membrane, Chem. Eng. J. 389 (February) (2020), https://doi.org/10.1016/j.cej.2020.124375.

[31] A. Milev, M. Wilson, G.S.K. Kannangara, N. Tran, X-ray diffraction line profile analysis of nanocrystalline graphite, Mater. Chem. Phys. 111 (2–3) (2008) 346–350, https://doi.org/10.1016/j.matchemphys.2008.04.024.

[32] C. Botas, et al., The effect of the parent graphite on the structure of graphene oxide, Carbon N. Y. 50 (1) (2012) 275–282, https://doi.org/10.1016/j.carbon.2011.08.045.

[33] G.K. Ayyadurai, G. Kittappa, P. Emerson, G.K. Rajendran, S. Srinivasan, B. M. Gunasekaran, Ultrasonication accelerated covalently grafted piperazine on reduced graphene oxide via nucleophilic substitution reaction for electrochemical supercapacitor electrode material, J. Mol. Struct. 1337 (2025) 142247, https://doi.org/10.1016/j.molstruc.2025.142247.

[34] F.S. AlHumaidan, M.S. Rana, Determination of asphaltene structural parameters by Raman spectroscopy, J. Raman Spectrosc. 52 (11) (2021) 1878–1891, https://doi.org/10.1002/jrs.6233.

[35] M.R. Baldan, E.C. Almeida, A.F. Azevedo, E.S. Gonçalves, M.C. Rezende, N. G. Ferreira, Raman validity for crystallite size L a determination on reticulated vitreous carbon with different graphitization index, Appl. Surf. Sci. 254 (2) (2007) 600–603, https://doi.org/10.1016/j.apsusc.2007.06.038.

[36] M.A. Pimenta, G. Dresselhaus, M.S. Dresselhaus, L.G. Cançado, A. Jorio, R. Saito, Studying disorder in graphite-based systems by Raman spectroscopy, Phys. Chem. Chem. Phys. 9 (11) (2007) 1276–1291, https://doi.org/10.1039/b613962k.

[37 N.M.S. Hidayah, et al., Comparison on graphite, graphene oxide and reduced graphene oxide: Synthesis and characterization, AIP Conf. Proc. 1892 (2017), https://doi.org/10.1063/1.5005764.

[38] A.Y. Lee, et al., Raman study of D* band in graphene oxide and its correlation with reduction, Appl. Surf. Sci. 536 (September 2020) (2021) 147990, https://doi.org/10.1016/j.apsusc.2020.147990.

[39] B. Lesiak, et al., Chemical and structural properties of reduced graphene oxide—dependence on the reducing agent, J. Mater. Sci. 56 (5) (2021) 3738–3754, https://doi.org/10.1007/s10853-020-05461-1.

[40] T.D. Dao, H.M. Jeong, Graphene prepared by thermal reduction-exfoliation of graphite oxide: Effect of raw graphite particle size on the properties of graphite oxide and graphene, Mater. Res. Bull. 70 (2015) 651–657, https://doi.org/10.1016/j.materresbull.2015.05.038.

[41 C. Pardanaud, et al., In-plane and out-of-plane defects of graphite bombarded by H, D and He investigated by atomic force and Raman microscopies, J. Raman Spectrosc. 46 (2) (2015) 256–265, https://doi.org/10.1002/jrs.4624.

[42] A.J. Pollard, et al., Quantitative characterization of defect size in graphene using Raman spectroscopy, Appl. Phys. Lett. 105 (25) (2014), https://doi.org/10.1063/1.4905128.

[43] Y. Zhang, W. Hu, B. Li, C. Peng, C. Fan, Q. Huang, Synthesis of polymer-protected graphene by solvent-assisted thermal reduction process, Nanotechnology 22 (34) (2011), https://doi.org/10.1088/0957-4484/22/34/345601.

[44] X. Liu, S. Shanbhag, S. Natesakhawat, J.F. Whitacre, M.S. Mauter, Performance Loss of Activated Carbon Electrodes in Capacitive Deionization: Mechanisms and

Material Property Predictors, Environ. Sci. Technol. 54 (23) (2020) 15516–15526, https://doi.org/10.1021/acs.est.0c06549.
[45] K. Fan, C. Gong, T. Peng, J. Chen, J. Xia, A novel preparation of small TiO2 nanoparticle and its application to dye-sensitized solar cells with binder-free paste at low temperature, Nanoscale 3 (9) (2011) 3900–3906, https://doi.org/10.1039/c1nr10481k.
[46] L.H. Kao, Y.P. Chen, Characterization, photoelectrochemical properties, and surface wettabilities of transparent porous TiO2 thin films, J. Photochem. Photobiol. A Chem. 340 (2017) 109–119, https://doi.org/10.1016/j.jphotochem.2017.03.011.
[47] J. Ma, M. Xing, L. Yin, K. San Hui, K.N. Hui, Porous hierarchical TiO2/MoS2/RGO nanoflowers as anode material for sodium ion batteries with high capacity and stability, Appl. Surf. Sci. 536 (August 2020) (2021) 147735, https://doi.org/10.1016/j.apsusc.2020.147735.
[48] N. Kularatna, pdf, Supercapacitor Energy Storage Sol. Appl. (2015) 1308–1312.
[49] T.N.J.I. Edison, et al., Electrochemically exfoliated graphene sheets as electrode material for aqueous symmetric supercapacitors, Surf. Coat. Technol. 416 (April) (2021) 127150, https://doi.org/10.1016/j.surfcoat.2021.127150.
[50] B. Dyatkin, et al., Influence of Surface Oxidation on Ion Dynamics and Capacitance in Porous and Nonporous Carbon Electrodes, J. Phys. Chem. C. 120 (16) (2016) 8730–8741, https://doi.org/10.1021/acs.jpcc.6b01204.
[51] N. Wang, G. Han, Y. Xiao, Y. Li, H. Song, Y. Zhang, Polypyrrole/graphene oxide deposited on two metalized surfaces of porous polypropylene films as all-in-one flexible supercapacitors, Electrochim. Acta 270 (2018) 490–500, https://doi.org/10.1016/j.electacta.2018.03.090.
[52] Y. Yoon, et al., Vertical alignments of graphene sheets spatially and densely piled for fast ion diffusion in compact supercapacitors, ACS Nano 8 (5) (2014) 4580–4590, https://doi.org/10.1021/nn500150j.
[53] J. Shabani Shayeh, A. Ehsani, M.R. Ganjali, P. Norouzi, B. Jaleh, Conductive polymer/reduced graphene oxide/Au nano particles as efficient composite materials in electrochemical supercapacitors, Appl. Surf. Sci. 353 (2015) 594–599, https://doi.org/10.1016/j.apsusc.2015.06.066.
[54] A. Śliwak, B. Grzyb, N. Díez, G. Gryglewicz, Nitrogen-doped reduced graphene oxide as electrode material for high rate supercapacitors, Appl. Surf. Sci. 399 (2017) 265–271, https://doi.org/10.1016/j.apsusc.2016.12.060.
[55] C. Zhao, P. Ju, S. Wang, Y. Zhang, S. Min, X. Qian, One-step hydrothermal preparation of TiO2/RGO/Ni(OH)2/NF electrode with high performance for supercapacitors, Electrochim. Acta 218 (2016) 216–227, https://doi.org/10.1016/j.electacta.2016.09.122.
[56] Y. Zhang, P.T. Cummings, Effects of Solvent Concentration on the Performance of Ionic-Liquid/Carbon Supercapacitors, ACS Appl. Mater. Interfaces (2019), https://doi.org/10.1021/acsami.9b09939.
[57] T. Liu, L. Zhang, B. Cheng, X. Hu, J. Yu, Holey Graphene for Electrochemical Energy Storage, Cell Rep. Phys. Sci. 1 (10) (2020) 100215, https://doi.org/10.1016/j.xcrp.2020.100215.
[58] Z. Niu, Y. Zhang, Y. Zhang, X. Lu, J. Liu, Enhanced electrochemical performance of three-dimensional graphene/carbon nanotube composite for supercapacitor application, J. Alloy. Compd. 820 (2020) 153114, https://doi.org/10.1016/j.jallcom.2019.153114.
[59] Z. Fan, J. Zhu, X. Sun, Z. Cheng, Y. Liu, Y. Wang, High Density of Free-Standing Holey Graphene/PPy Films for Superior Volumetric Capacitance of Supercapacitors, ACS Appl. Mater. Interfaces 9 (26) (2017) 21763–21772, https://doi.org/10.1021/acsami.7b03477.
[60] W. Liu, G. Speranza, Tuning the Oxygen Content of Reduced Graphene Oxide and Effects on Its Properties, ACS Omega 6 (9) (2021) 6195–6205, https://doi.org/10.1021/acsomega.0c05578.
[61] B.G. Choi, J. Hong, W.H. Hong, P.T. Hammond, H. Park, Facilitated ion transport in all-solid-state flexible supercapacitors, ACS Nano 5 (9) (2011) 7205–7213, https://doi.org/10.1021/nn202020w.
[62] S. Dai, et al., A high-performance supercapacitor electrode based on N-doped porous graphene, J. Power Sources 387 (2018) 43–48, https://doi.org/10.1016/j.jpowsour.2018.03.055.
[63] H.Zhang Deyi, Hao Yuan, Zheng Liwen, Ma Ying, Feng Huixia, Luo, 美国科学院学报 Materials Chemistry A 材料化学 a, J. Mater. Chem. A 1 (207890) (2013) 7584–7591.
[64] H. Shen, et al., High-performance aqueous symmetric supercapacitor based on polyaniline/vertical graphene/Ti multilayer electrodes, Electrochim. Acta 283 (2018) 410–418, https://doi.org/10.1016/j.electacta.2018.06.182.
[65] J.J. Yoo, et al., Ultra Planar Graph. Supercapacitors (2011) 1423–1427.
[66] F. Liu, S. Song, D. Xue, H. Zhang, Folded structured graphene paper for high performance electrode materials, Adv. Mater. 24 (8) (2012) 1089–1094, https://doi.org/10.1002/adma.201104691.
[67] Z. Weng, Y. Su, D.W. Wang, F. Li, J. Du, H.M. Cheng, Graphene-cellulose paper flexible supercapacitors, Adv. Energy Mater. 1 (5) (2011) 917–922, https://doi.org/10.1002/aenm.201100312.
[68] M.R. Saeb, P. Zarrintaj, Polyaniline/graphene-based nanocomposites, Elsevier Inc, 2019, https://doi.org/10.1016/B978-0-12-817915-4.00010-5.
[69] Q. Wu, Y. Xu, Z. Yao, A. Liu, G. Shi, Supercapacitors based on flexible graphene/polyaniline nanofiber composite films, ACS Nano 4 (4) (2010) 1963–1970, https://doi.org/10.1021/nn1000035.
[70] Z. Niu, et al., Electrophoretic build-up of alternately multilayered films and micropatterns based on graphene sheets and nanoparticles and their applications in flexible supercapacitors, Small 8 (20) (2012) 3201–3208, https://doi.org/10.1002/smll.201200924.
[71] Y. Wang, et al., Graphene/carbon black hybrid film for flexible and high rate performance supercapacitor, J. Power Sources 271 (2014) 269–277, https://doi.org/10.1016/j.jpowsour.2014.08.007.
[72] R. Thangavel, et al., High-energy green supercapacitor driven by ionic liquid electrolytes as an ultra-high stable next-generation energy storage device, J. Power Sources 383 (January) (2018) 102–109, https://doi.org/10.1016/j.jpowsour.2018.02.037.
[73 J.L. Shamshina, P. Berton, Renewable Biopolymers Combined with Ionic Liquids for the Next Generation of Supercapacitor Materials, Int. J. Mol. Sci. 24 (9) (2023), https://doi.org/10.3390/ijms24097866.
[74] B.A. Mei, O. Munteshari, J. Lau, B. Dunn, L. Pilon, Physical Interpretations of Nyquist Plots for EDLC Electrodes and Devices, J. Phys. Chem. C. 122 (1) (2018) 194–206, https://doi.org/10.1021/acs.jpcc.7b10582.
[75] B.A. Mei, J. Lau, T. Lin, S.H. Tolbert, B.S. Dunn, L. Pilon, Physical Interpretations of Electrochemical Impedance Spectroscopy of Redox Active Electrodes for Electrical Energy Storage, J. Phys. Chem. C. 122 (43) (2018) 24499–24511, https://doi.org/10.1021/acs.jpcc.8b05241.
[76] J.P. Diard, J.M. Le Canut, B. Le Gorrec, C. Montella, Copper electrodissolution in 1 M HCl at low current densities. I. General steady-state study, Electrochim. Acta 43 (16–17) (1998) 2469–2483, https://doi.org/10.1016/S0013-4686(97)10155-4.
[77] X. Ren, P.G. Pickup, An impedance study of electron transport and electron transfer in composite polypyrrole + polystyrenesulphonate films, J. Electroanal. Chem. 420 (1–2) (1997) 251–257, https://doi.org/10.1016/S0022-0728(96)04784-5.
[78] K. Chen, S. Song, F. Liu, D. Xue, Structural design of graphene for use in electrochemical energy storage devices, Chem. Soc. Rev. 44 (17) (2015) 6230–6257, https://doi.org/10.1039/c5cs00147a.
[79] Z. Chen, Z. Li, X. Ma, Y. Wang, Q. Zhou, S. Zhang, A new DMF-derived ionic liquid with ultra-high conductivity for high-capacitance electrolyte in electric double-layer capacitor, Electrochim. Acta 319 (2019) 843–848, https://doi.org/10.1016/j.electacta.2019.07.015.
[80] A. Mery, F. Ghamouss, C. Autret, D. Farhat, F. Tran-Van, Aqueous ultracapacitors using amorphous MnO2 and reduced graphene oxide, J. Power Sources 305 (2016) 37–45, https://doi.org/10.1016/j.jpowsour.2015.11.046.